Anisotropic anomalous transport in the kagome-based topological antiferromagnetic math xmlns="http://www.w3.org/1998/Math/MathML">msub>mi mathvariant="normal">Mn/mi>mn>3/mn>/msub>mtext> Ga/mtext>/math> epitaxial thin films

M. Raju, Ralph Romero, III, Daisuke Nishio-Hamane, Ryota Uesugi, Mihiro Asakura, Zhenisbek Tagay, Tomoya Higo, N. P. Armitage, Collin Broholm, and Satoru Nakatsuji

Phys. Rev. Materials **8**, 014204 — Published 26 January 2024

DOI: 10.1103/PhysRevMaterials.8.014204

Anisotropic anomalous transport in the kagome-based topological antiferromagnetic Mn_3Ga epitaxial thin films

M. Raju[1†], Ralph Romero III[1], Daisuke Nishio-Hamane[4], Ryota Uesugi[2,3], Mihiro Asakura[2], Zhenisbek Tagay[1], Tomoya Higo[2,3,4], N.P. Armitage[1,5], Collin Broholm[1], and Satoru Nakatsuji[1,2,3,4,5*]

[1] *Institute for Quantum Matter, Department of Physics and Astronomy, Johns Hopkins University, Baltimore, MD 21218, USA*

[2] *Department of Physics, University of Tokyo, Bunkyo-ku, Tokyo, Japan.*

[3] *Institute for Solid State Physics, University of Tokyo, Kashiwa, Chiba, Japan.*

[4] *Trans-scale Quantum Science Institute, University of Tokyo, Bunkyo-ku, Tokyo, Japan.*

[5] *Canadian Institute for Advanced Research (CIFAR), Toronto, Ontario M5G 1M1, Canada.*

Mn_3X(X=Sn, Ge, Ga) kagome Weyl semimetals have attracted significant research interest due to their large anomalous Hall, thermal, and optical effects originating from their non-trivial band topology. These large topological effects together with the antichiral antiferromagnetic order that can be manipulated through various experimental means provide unique platforms for developing high-speed spintronics. Mn_3Ga is known to have the largest Neél temperature ($T_N \approx 480$ K), which is useful for developing antiferromagnetic spintronics. Here, we establish the epitaxial growth of antiferromagnetic Mn_3Ga films by magnetron sputtering and present their structural, magneto-transport, terahertz properties, and exchange-bias effect in Mn_3Ga/NiFe bilayers, establishing its remarkable properties essential for future investigations towards device applications.

I. INTRODUCTION

Weyl semimetal Mn_3X(X=Sn, Ge, Ga) compounds hosting antichiral spin structure on their kagome lattices have attracted research interest for their fascinating properties useful for developing antiferromagnetic (AFM) topological spintronics[1–4]. These materials show large nontrivial effects such as anomalous Hall effect (AHE)[5] up into the THz frequency range[6], spin Hall and magnetic spin Hall effects[7], anomalous Nernst effect (ANE)[8, 9] and magneto-optical effects[6, 10–12]. These electromagnetic responses originate from a sizable momentum space Berry curvature, linked to the chiral AFM spin texture formed by the Mn spin moments on the Mn kagome lattice in real space. This coupling of real space spin structure to the momentum space band topology provides a necessary handle to harness the technological prospects of these materials[3, 13, 14]. Hexagonal Mn_3X materials show anisotropic magneto-transport responses along different crystal orientations as well as kagome spin structure formed by the Mn moments[13, 15–17], hence, control over crystal orientation in thin films structures is essential to fully exploit the Berry phase effects for device applications. For example, it is desirable to have the kagome spin structure aligned normal to the film plane, that is *ab*-axis orientation, for spintronics devices based on AHE[18, 19], and kagome spin structure within the film plane, which is *c*-axis orientation, for devices based on spin Hall or thermoelectric effects[7, 20]. Recent experimental successes in the electrical and optical detection/manipulation of antiferromagnetic order using Mn_3Sn thin films are promising towards developing antiferromagnetic random access memory[18, 19, 21–24]. In addition, recent observations on superconducting proximity effects in Mn_3Ge/Nb interfacial system open new possibilities of topological superconducting spintronics[25].

Within the family of the hexagonal $D0_{19}$ Mn_3X(X=Sn,Ge,Ga) compounds, so far Mn_3Ga has attracted limited attention compared to Mn_3Sn and Mn_3Ge, probably due to a smaller anomalous Hall conductivity (AHC) reported for this material[15, 26, 27] and growth challenges due to competing Mn-Ga structural and magnetic phases[27]. The hexagonal Mn_3Ga is expected to be an antiferromagnetic Weyl semimetal with a larger spin Hall response[15] and is known to have a larger magnetic ordering temperature ($T_N \approx 480$ K) compared to $T_N \approx 420$ K and $T_N \approx 360$ K of Mn_3X(X=Sn,Ge), respectively.

For memory applications, which is the ultimate and realistic goal of electrical switching, higher magnetic transition temperatures are required in terms of thermal stability. In light of this, developing a similar class of thin film materials with the largest possible T_N, like antiferromagnetic Mn_3Ga, is an essential requirement. In this work, we develop the hexagonal Mn_3Ga AFM thin films by using the magnetron sputtering technique. We use MgO(110) substrates with W(7 nm) buffer layer for achieving *ab*-axis oriented Mn_3Ga and Al_2O_3(0001) substrates with Ru(5 nm) buffer layer for *c*-axis ori-

* Correspondence:
† mraju5@jhu.edu; *snakats1@jhu.edu

ented Mn_3Ga films. Films are characterized through X-ray diffraction (XRD), cross-sectional high-resolution transmission electron microscopy (HRTEM), magnetization measurements, AHE, magnetoresistance (MR) effect, and THz Faraday effect. Our investigations reveal that both *ab*-axis and *c*-axis films grow epitaxially, albeit the *ab*-axis Mn_3Ga films show minor peak corresponding to $(31\bar{4}0)$ oriented crystallites. Films have in-plane strain up to 0.7% and 1.6% depending on the substrate and the buffer layer. The *ab*-axis orientated Mn_3Ga shows large spontaneous AHE, which vanishes for the *c*-axis case, confirming the expected anisotropy in AHE for these two crystal orientations [15]. The AHE magnitude for the *ab*-axis case shows a non-monotonic behavior with temperature, with an estimated AHC of 17 $(\Omega\text{cm})^{-1}$ at 300 K, 28 $(\Omega\text{cm})^{-1}$ between 100-200 K and 19 $(\Omega\text{cm})^{-1}$ at 10 K. The THz time-domain spectroscopy investigations between 10-225 K reveal a large Faraday effect, consistent with the AHE trends seen in the DC transport measurements and THz optical properties comparable to previously reported Mn_3Sn films [28]. The MR measurements show an increase in negative magnetoresistance (NMR) for the applied field (B) parallel to current (I), B∥I, compared to B⊥I configuration, suggestive of chiral anomaly behavior expected for this class of materials. Finally, we demonstrate the exchange bias effect in Mn_3Ga(40 nm)/NiFe(10 nm) establishing the antiferromagnetic character of our hexagonal Mn_3Ga films, these results provide insights into the effect of Mn_3Ga(40 nm) crystal orientation on exchange bias properties.

II. RESULTS AND DISCUSSION

II.1. Structural characterization

Figures 1a, 1g show the schematics of the sample structure MgO(110)/W(7 nm)/Mn_3Ga(40 nm)/AlO-cap, Al_2O_3(0001)/Ru(5 nm)/Mn_3Ga(40 nm)/AlO-cap used in this work for *ab*-axis, *c*-axis oriented Mn_3Ga, respectively, and the expected antichiral spin structure formed by Mn moments along the out-of-plane direction. Figures 1b-1c, and 1h-1i show the results obtained by the X-ray diffraction investigations. A combination of out-of-plane and in-plane diffraction peaks captured in the Figs. 1b-1c and 1h-1i confirm the epitaxial growth of the films with *ab*-axis orientaion on MgO/W and *c*-axis orientation on Al_2O_3/Ru. Rocking curve measurements are carried out on each diffraction peak to assess their width (see Figure S1, Supplementary Material [29]). All the diffraction peaks can be identified uniquely with the hexagonal Mn_3Ga phase, indicating a single phase without any impurity phases.

In the case of the *ab*-axis oriented film, along with $(02\bar{2}0)$ $(2\theta = 38.612°)$ and $(04\bar{4}0)(2\theta = 82.656°)$ diffraction peaks we also see a minor peak corresponding to $(31\bar{4}1)(2\theta = 77.478°)$, suggesting the presence of undesired crystallites. On the other hand, our *c*-axis films show only $(0002)(2\theta = 41.464°)$ and $(0004)(2\theta = 90.035°)$ diffraction peaks. Width of the diffraction peaks (see Figure S1, Supplementary Material [29]) suggests *c*-axis oriented films (FWHM=0.006°) have superior quality compared to *ab*-axis films (FWHM=1.3°), these structural differences are influenced by the underlying buffer layers, larger width of $Mn_3Ga(02\bar{2}0)$ diffraction peaks correlates with the larger width of the W(7 nm) (FWHM=1.9°) layer diffraction peaks, and sharper diffraction peaks for *c*-axis $Mn_3Ga(0002)$ correlates well with the sharper diffraction peaks of Ru(5 nm) (FWHM=0.005°) layer.

Based on $(02\bar{2}0)$ and $(20\bar{2}1)$ diffraction peaks of *ab*-axis oriented sample shown in Figs.1b-1c, our estimated lattice parameters indicate $a = 5.384$Å, and $c = 4.380$Å. In case of the *c*-axis oriented sample shown in Figs.1h-1i, diffraction peaks (0002), and $(20\bar{2}3)$ lead to estimated lattice parameters of $a = 5.306$Å, and $c = 4.355$Å. Comparison of the estimated values with lattice parameters of a bulk hexagonal Mn_3Ga compound, $a^{bulk} = 5.391$Å, $c^{bulk} = 4.348$Å[30] shows that our Mn_3Ga films on MgO(110)/W(7 nm) show an estimated in-plane tensile strain $(\frac{|(c^{film}-c^{bulk})|}{c^{bulk}}\times 100)$ of $\approx 0.7\%$ and an out-of-plane compressive strain $((\frac{|(a^{film}-a^{bulk})|}{a^{bulk}}\times 100))$ of $\approx 0.1\%$. On the other hand, Mn_3Ga films on $Al_2O_3(0001)$/Ru(5 nm) show an in-plane compressive strain $((\frac{|(a^{film}-a^{bulk})|}{a^{bulk}}\times 100))$ of $\approx$ 1.6% and an out-of-plane tensile strain $(\frac{|(c^{film}-c^{bulk})|}{c^{bulk}}\times 100)$ of $\approx 0.1\%$. These observations suggest that underlying buffer layers play a key role in in-plane lattice strain in the subsequently grown Mn_3Ga films. Studies have shown that the strain in these thin film structures plays an important role in controlling the effective magnetic anisotropy and electrical control of magnetic moments[19, 31, 32].

Development of *ab*-axis oriented Mn_3X epitaxial films had been a challenge, almost all the works so far were focused on Mn_3Sn, often requiring high-temperature treatment for epitaxial growth, and a buffer layer with appropriate lattice matching is essential to promote hexagonal structure. One needs to find an optimum temperature to promote crystal growth without causing the intermixing of elements at the interface with the buffer layer [19, 33]. A small volume fraction of unwanted crystal orientations is expected for the annealing temperatures used in this work[19]. The presence of crystal grains with different orientations may produce interesting magnetotransport in these materials. For example, the volume fraction of the grains with a kagome plane normal to the film surface contribute largely to the anomalous Hall signal, while grains with a kagome plane within the film produce spin Hall effect, which may lead to self-switching spin-polarized current[22].

Figures 1d-1f and 1j-1l show the results of the HRTEM investigations for the films on the MgO and Al_2O_3 substrates, respectively. As shown in Fig.1e, electron diffraction of MgO, W, and Mn_3Ga and their simulated patterns [34] show epitaxial growth with the crystal orientation of $MgO(110)[00\bar{1}]||W(211)[01\bar{1}]||Mn_3Ga(01\bar{1}0)[000\bar{1}]$.

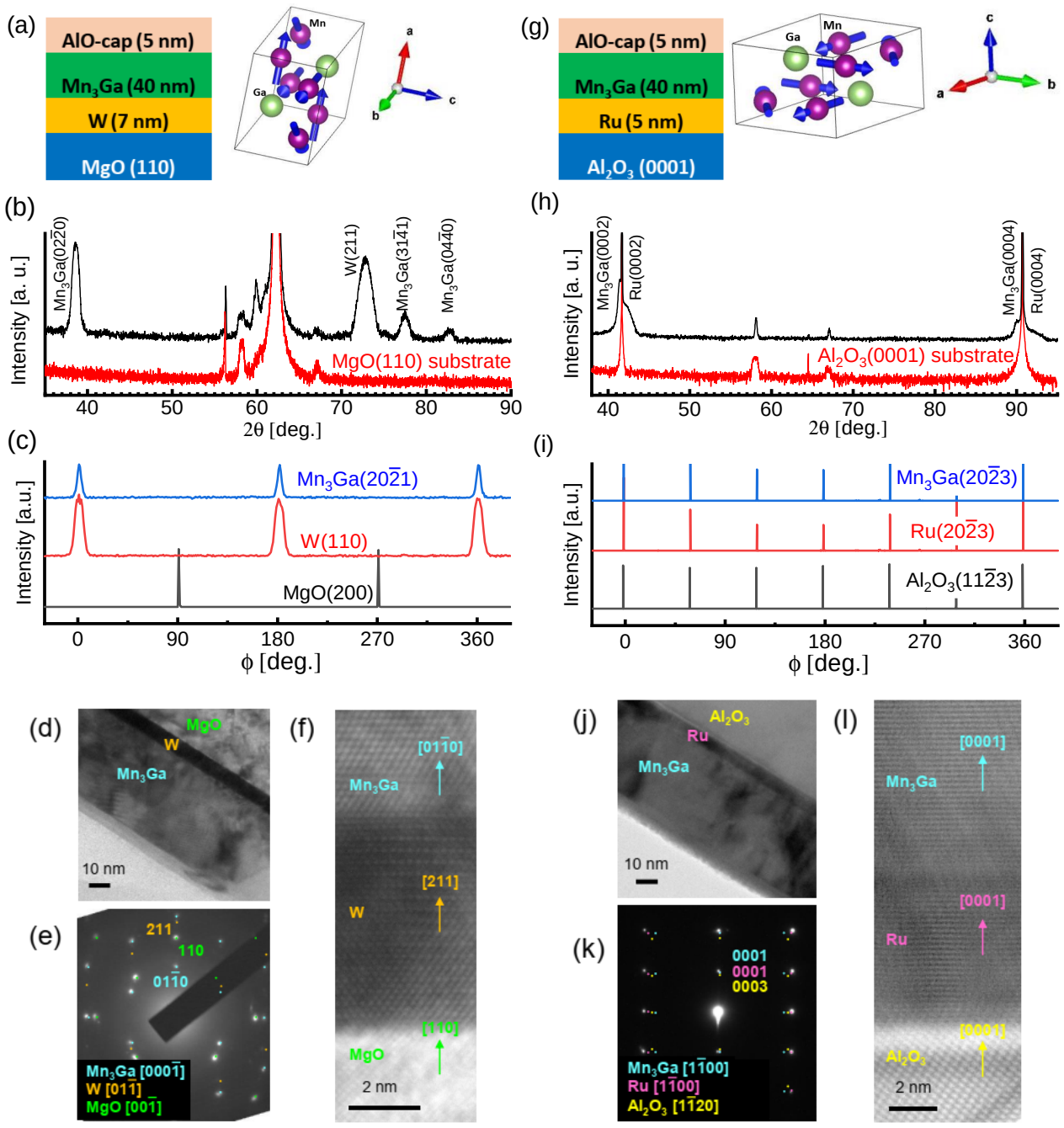

FIG. 1. **X-ray diffraction and cross-sectional HRTEM results for the *ab*-axis and *c*-axis oriented Mn_3Ga samples**. Schematics for thin film stacks and antichiral spin structures expected, **(a)** for the *ab*-axis oriented Mn_3Ga film stack, i.e. MgO(110)/W(7 nm)/Mn_3Ga(40 nm)/Al_2O_3(5 nm) and **(g)** for the *c*-axis oriented Mn_3Ga film stack Al_2O_3(0001)/Ru(5 nm)/Mn_3Ga(40 nm)/Al_2O_3(5 nm). **(b-c)** $\theta-2\theta$ and in-plane ϕ-scans for the *ab*-axis oriented Mn_3Ga(40 nm) film. **(d-f)** Cross-sectional view of the HRTEM sample, experimental and simulated electron diffraction patterns and cross-sectional high-resolution TEM image for *ab*-axis oriented Mn_3Ga(40 nm) film. **(h-i)** $\theta-2\theta$ and in-plane ϕ-scans of the *c*-axis oriented Mn_3Ga(40 nm) film. $\theta-2\theta$ scans for bare MgO(110) and Al_2O_3(0006) substrates shown in panel (b) and (h) are also recorded for reference. **(j-l)** Cross-sectional view of the HRTEM sample, experimental and simulated electron diffraction patterns and cross-sectional high-resolution TEM image for *c*-axis oriented Mn_3Ga(40 nm) film.

Similarly, in Fig. 1k, the electron diffraction patterns of the film on the Al_2O_3 substrates show crystal orientation $Al_2O_3(0001)[00\bar{1}]||Ru(0001)[0\bar{1}1]||Mn_3Ga(0001)[11\bar{2}0]$. These electron diffraction results and the cross-section images shown in Figs.1f and 1l are consistent with the XRD investigations. The electron diffraction patterns of Al_2O_3 and Ru, Mn_3Ga overlap (Fig.1k), although it is difficult to distinguish the patterns for each layer, we

expect the film to be oriented consistent with the XRD results since no extra diffraction spots are seen.

II.2. Magnetization

Figure 2 shows the magnetization data for both *ab*-axis oriented Mn_3Ga grown on MgO/W and *c*-axis oriented Mn_3Ga on Al_2O_3/Ru, recorded in out-of-plane applied field. Magnetization for the *ab*-axis sample is shown to be relatively larger compared to the *c*-axis sample. As a function of the field, a smooth variation of magnetization with a coercivity of 0.01 T is seen for the *c*-axis case while the *ab*-axis shows a coercivity of 0.1 T (inset to Fig.2a). These observations are consistent with the expected anisotropy in magnetization along these crystal orientations. However, an estimated spontaneous magnetic moment suggests a moment up to $\approx 0.042\ \mu_B/Mn$ for *ab*-axis-oriented film and $\approx 0.016\ \mu_B/Mn$ for *c*-axis-oriented film, several times larger compared to few milli μ_B/Mn expected for their bulk crystal forms[26]. Such an enhancement in magnetization appears to be common in similar non-collinear antiferromagnetic thin films[35], probably caused by several factors such as chemical, structural disorder, and demagnetization effects in the thin film limit[19, 31, 32, 35]. In fact, increased magnetic moment and anisotropy may also result from the lattice strain in the film leading to piezomagnetic effects [36]. Figure 2b shows the temperature-dependent in-plane magnetization measured between 300-600 K. Samples were first magnetized by applying an in-plane field of 5 T and then the field was reduced to zero. The measured remnant magnetization with temperature suggests a T_N of ≈ 485 K for both *ab*-axis and *c*-axis oriented samples grown on different substrates. This measured T_N further confirms the phase purity of our hexagonal antiferromagnetic Mn_3Ga films. The T-dependent magnetization data in Fig.2c shows that the *ab*-axis samples possess a larger magnetization compared to *c*-axis films for the entire temperature range of 10-400 K. Further, *ab*-axis oriented films show subtle dip-like variation in magnetization around 175 K, followed by a broad shallow peak around 150 K. These variations are highlighted through a numerical derivative of magnetization (dM/dT) with T as shown in Fig.2d. This feature in *ab*-axis magnetization may be associated with the distortion from hexagonal to orthorhombic structure expected for this material system[26, 37, 38]. In-plane lattice distortion in ab-axis oriented sample is expected to produce spin canting away from the kagome-plane which may result in reduced magnetization within the kagome-plane. However, a similar feature is absent for *c*-axis films. In our opinion, such structural distortions and resulting changes in magnetization may easily be masked by substrate-induced lattice strain in the epitaxial thin films at reduced thicknesses[39], lattice strain up to $0.7 - 1.6\%$ estimated for our films may have a significant effect on the structural and magnetic behavior of thin film Mn_3Ga.

For c-axis case shown in Fig.2c, ZFC curve shows a decreasing magnetization with reducing temperature, whereas FC curve shows an increasing magnetization which tends to saturate at low temperatures. On the other hand, for ab-axis orientation, both ZFC and FC curves show increasing magnetization with decreasing temperature, these ZFC-FC observations along *c*-axis and *ab*-axis crystal orientation are consistent with previous reports on similar hexagonal Mn_3X systems [26, 38, 40]. The anisotropy in low field ZFC-FC behavior along *ab*-axis and *c*-axis may point to the anisotropic nature of magnetic interactions and the strain effects along these crystal directions[36, 41, 42].

II.3. DC and THz Anomalous Hall effect

The chiral antiferromagnets Mn_3Sn and Mn_3Ge are known to show anisotropic magnetotransport under magnetic fields along different crystal orientations[5, 13, 43, 44]. Non-zero spontaneous AHE arises when the applied field is along the *ab*-axis (within the kagome plane formed by Mn moments with antichiral spin structure), while it vanishes for the field along *c*-axis. Control over crystal orientation established in our films enables verification of such anisotropic transport signatures for our Mn_3Ga films. Figure 3a shows a comparison of AHE at 300 K for *ab*-axis and *c*-axis oriented samples. The *ab*-axis oriented film shows a non-zero spontaneous AHE while it disappears for *c*-axis orientation. This anisotropic behavior persists for the entire temperature range of the measurements 10-400 K. The temperature sweep measurements using the *ab*-axis oriented samples reveal that AHE shows a non-monotonic behavior. In order to estimate the AHC ($\sigma_{yx} = -\rho_{yx}/\rho_{xx}^2$) of the Mn_3Ga(40 nm) layer, we estimate the anomalous Hall ($\rho_{yx}^{Mn_3Ga}$) and longitudinal resistivity ($\rho_{xx}^{Mn_3Ga}$) corresponding to Mn_3Ga(40 nm) layer, shown in Fig.3b, by accounting for the electrical current shunting through the W(7 nm) buffer layer[19]. In Fig.3c we combine the measurements performed in PPMS and a custom-built high-temperature probe to track the high-temperature evolution of the $\rho_{yx}^{Mn_3Ga}(T)$ up to $\approx$500 K. Our data suggests $\rho_{yx}^{Mn_3Ga}(T)$ approaches zero value at ≈ 480 K, confirming the expected T_N for our films, consistent with the T_N estimated from magnetization measurements shown in Fig.2b. Due to temperature limitations in our custom-built high-temperature probe we are unable to verify the AHE beyond 500 K. One expects the AHE to saturate close to zero value for temperature beyond T_N, such behavior may also be witnessed in magnetization, which we verify in Fig.2b.

The temperature dependence of the zero-field $\sigma_{yx}(T)$ estimated from the data in panel 3b is summarized in Fig.3d. As shown, $-\sigma_{yx}(T)$ starts with 19 $(\Omega\text{cm})^{-1}$ at 10 K, and goes through a maximum of 28 $(\Omega\text{cm})^{-1}$ between 100-200 K and decreases to 7 $(\Omega\text{cm})^{-1}$ with increasing temperature upto 400 K. A systematic decrease in $-\sigma_{yx}(T)$ for approaching 400 K is consistent with the behavior seen in $Mn_3X(X = \text{Sn, Ge})$[13, 18, 22, 45] systems where AHE is suppressed upon approaching T_N of

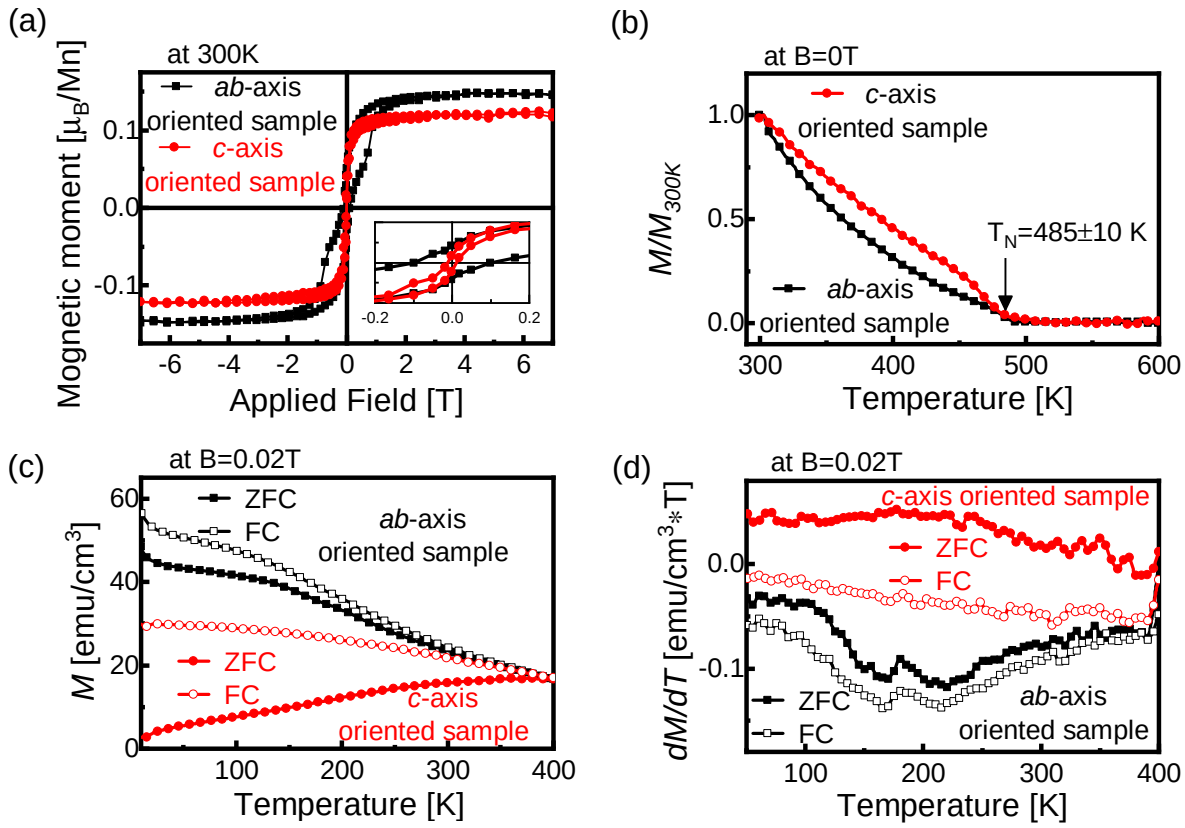

FIG. 2. **Magnetization results for the *ab*-axis and the *c*-axis-oriented Mn_3Ga films.(a)** Comparison of the magnetization vs. field (M(B)) curve measured at 300 K for *ab*-axis and *c*-axis oriented samples. Inset to the panel (a) shows the low field evolution of the M(B) curve. **(b)** In-plane magnetization vs. temperature (M(T)) measured between 300-600 K for *ab*-axis and *c*-axis oriented samples. Data is normalized to the magnetization value at 300 K, measurement is performed at B=0 T after saturating the sample at B=5 T. The error bar in the estimated value of Neél temperature represents uncertainty in the sample temperature. **(c)** Temperature dependence of the zero-field cooled (ZFC) and field cooled (FC) magnetization for the *ab*-axis and *c*-axis oriented Mn_3Ga samples, measured at B=0.02 T. **(d)** Numerical derivative dM/dT profiles of the M vs. T data shown in panel (c).

the materials

The sign of AHE in our films is consistent with experimental reports on Mn_3X(X=Sn, Ge)[13, 18, 19, 22, 45]. However, previous reports on Mn_3Ga have shown sign reversal for AHE including a transition to the behavior suggesting the topological Hall effect [26, 27, 38]. Such varying AHE signatures for Mn_3Ga indicate a sensitive role of the location of the Fermi-level in the band structure[15]. In contrast to the previous works, our work, particularly through AHE evolution up to 500 K, with an estimated $T_N \approx 480$ K establishes that a large AHC up to 28 $(\Omega\text{cm})^{-1}$ indeed emerges from the topological band structure of the antiferromagnetic hexagonal Mn_3Ga. Further, a persistent value of AHC $\approx$ 19 $(\Omega\text{cm})^{-1}$ at 10 K might suggest that Mn_3Ga sustains Weyl points in the vicinity of its Fermi level and anti-chiral antiferromagnetic phase down to low temperatures[37, 46], similar to Mn_3Ge and unlike Mn_3Sn which develops a spin-glass like behavior[5, 13]. Our high-quality Mn_3Ga films developed here, showing a large AHE and a large T_N, are ideal for clarifying the microscopic origin of electrical control of antiferromagnetic order in Mn_3X systems and their applications.

In Fig.3a, solid red lines highlight the field linear response of the $\rho_{yx}(B)$ for B>3 T. The estimated high field slope (0.03 ($\mu\Omega$cm/T)) for the *c*-axis orientation is about 4 times larger compared to the slope (0.007 ($\mu\Omega$cm/T)) for *ab*-axis orientation. Note that when the external field is applied along the *c*-axis, the Hall effect captures, along with the ordinary Hall effect, the AHE component from the scalar spin chirality emerging from the spin canting normal to the kagome plane formed by Mn moments. In such *c*-axis orientation, both ordinary and anomalous Hall components show linear field dependence, on the other hand, in the case of the *ab*-axis orientation, one can distinguish the dominant spontaneous AHE component from the field-linear term. Recent work on Mn_3Sn suggests that a large field-linear AHE in the *c*-axis orientation is a combined result of real and momentum space Berry phase[47].

To characterize THz AHE, we measure the complex transverse conductivity, $\sigma_{xy}(\omega)$ using time-domain terahertz spectrometer (TDTS) equipped with a 7 T superconducting magnet in a closed cycled helium cryostat.

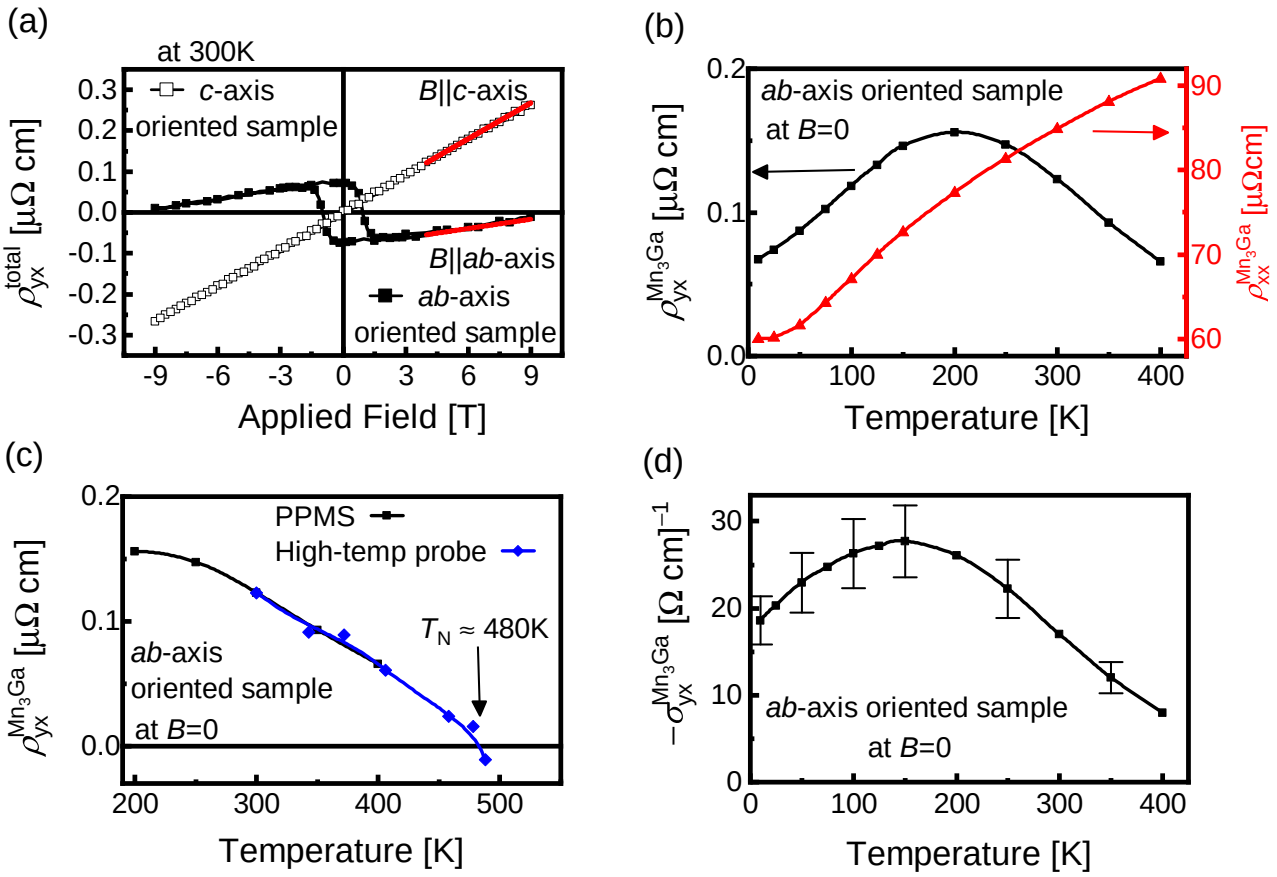

FIG. 3. **DC Anomalous Hall effect of ab-axis and c-axis oriented Mn_3Ga(40 nm) samples**. **(a)** Field dependent total DC Hall resistivity ($\rho_{yx}(B)$) of ab-axis and c-axis oriented Mn_3Ga(40 nm) samples recorded at 300 K. Red solid lines show a linear fit to the high field (4.5-9 T) Hall data highlighting the slope. **(b)** Temperature dependent DC Hall resistivity ($\rho_{yx}^{Mn_3Ga}(T)$) and longitudinal resistivity ($\rho_{xx}^{Mn_3Ga}(T)$) corresponding to ab-axis oriented Mn_3Ga at zero magnetic field. $\rho_{yx}^{Mn_3Ga}(T)$ and $\rho_{xx}^{Mn_3Ga}(T)$ are estimated by accounting for the current shunting through the W(7 nm) buffer layer[19].**(c)** High temperature evolution of $\rho_{yx}^{Mn_3Ga}(T)$, suggesting $\rho_{yx}^{Mn_3Ga} \approx 0$ at ≈480 K, which is close to the expected Néel temperature for Mn_3Ga. Square symbols refer to data measured in PPMS between 200-400 K, and diamond symbols refer to data measured in custom-built high-temperature probe between 300-500 K. **(d)** Estimated DC anomalous Hall conductivity ($\sigma_{yx} = -\rho_{yx}/\rho_{xx}^2$) from the data shown in the panel (b), error bars represent the possible variation in the estimated magnitude of σ_{yx}.

Figure 4a shows the schematic of our magneto TDTS setup. We generate the THz pulses using a TOPTICA TeraFlash Pro. This system irradiates an InGaAs photoconductive antenna (PCA) with 1550 nm pulses through a fiber optic cable. The PCA is effectively a gapped dipole antenna with a semiconductor bridging the gap. By applying a voltage across the semiconductor and irradiating the gap with an optical pulse whose photon energy matches the bandgap of the semiconductor, charge carriers are freed and accelerated by the external voltage which then recombine on picosecond timescales (1 ps = 1/1 THz). The radiated THz pulse is thus polarized parallel to the dipole antenna of the PCA as $E(t) \propto \frac{\partial j(t)}{\partial t}$, here we will define the initial polarization of the beam to be along the $\hat{x}$ direction. We then direct the THz beam using off-axis parabolic mirrors (OAPMs). We place the OAPMs in a so-called 8f geometry, as shown in Fig.4a. This geometry ensures a relatively frequency-independent, tight focus at the sample position. The magnetic sample then rotates the beam via the Faraday effect such that it is elliptically polarized. After the sample a wire grid polarizer (WGP) is placed such that it acts as a polarizing beam splitter, passing light polarized along $\hat{y}$ and reflecting light polarized along $\hat{x}$. The two beams are then focused onto separate detectors. This allows us to simultaneously measure $E_x(\omega)$ and $E_y(\omega)$. Noting that $E_x \gg E_y$, these quantities can be directly related to the complex Faraday rotation, θ_f, by $\theta_f(\omega) = \frac{E_y(\omega)}{E_x(\omega)}$. To eliminate any systematic effects that may manifest as finite rotations we carry out an antisymmetrization, where θ_f is averaged with opposite field values and then subtracted i.e. $\theta_{f,AS}(B) = \theta_f(B) - \left(\frac{\theta_f(B)+\theta_f(-B)}{2}\right)$. In Figs.4b-4d we focus on the THz optical AHE studied through $\theta_f(\omega)$ measured at different temperature. We use $\sigma_{xx}(\omega)$ and $\theta_f(\omega)$ to obtain $\sigma_{xy}(T)$ through the relation $\sigma_{xy} = \theta_f \left(\sigma_{xx} + \frac{n+1}{dZ_0}\right)$. Details of the THz conduc-

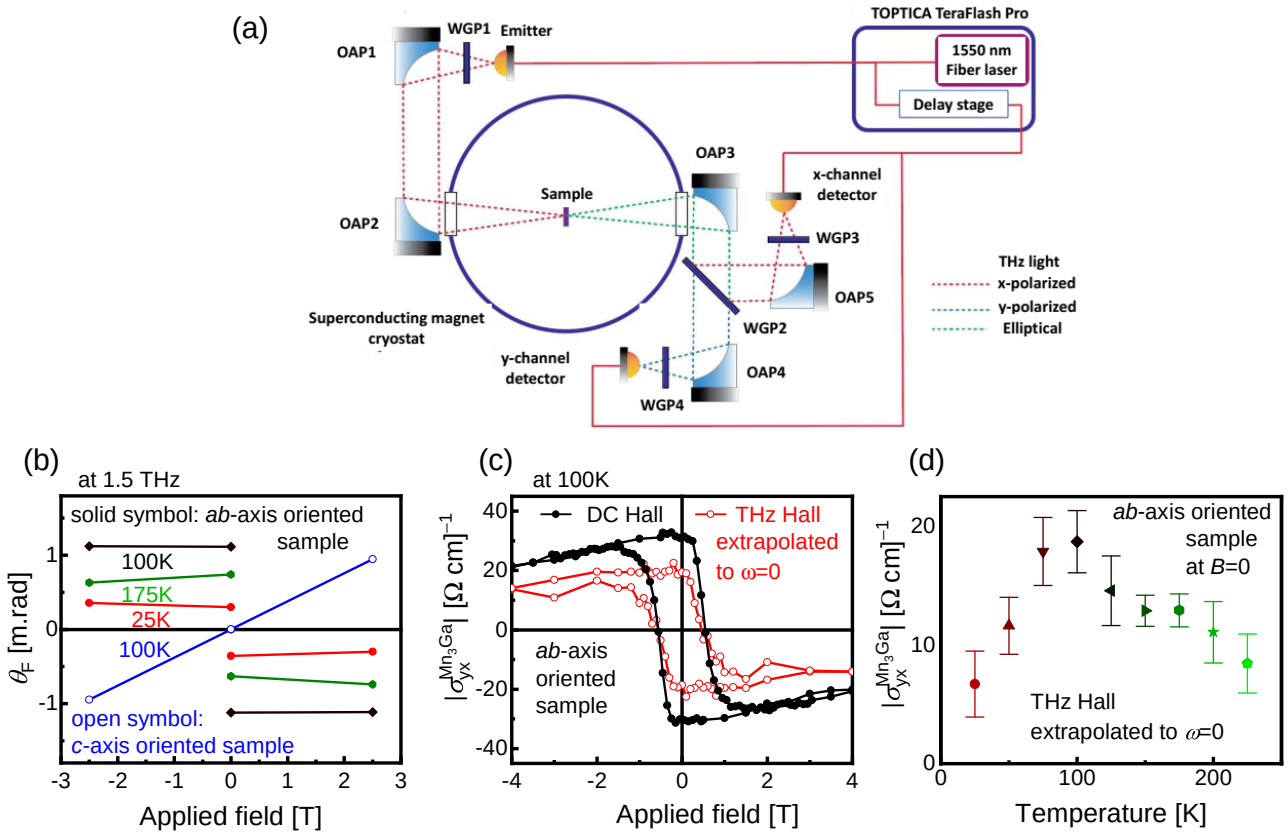

FIG. 4. **THz Anomalous Hall effect of *ab*-axis and *c*-axis oriented Mn_3Ga(40 nm) samples**. **(a)** Schematic of the magneto time-domain THz spectrometer used for measuring Faraday rotation. **(b)** THz Faraday rotation for *ab*-axis and *c*-axis oriented Mn_3Ga samples recorded at various fixed temperatures and frequency of 1.5 THz, as the applied field is reduced to zero from ±2.5 T. **(c)** Field evolution of THz Hall conductivity (estimated from field evolution of Faraday rotation) and its comparison with DC anomalous Hall conductivity for *ab*-axis Mn_3Ga sample recorded at 100 K. For comparison, the THz Hall data is extrapolated to $\omega = 0$ (see Figure S3, Supplementary Material [29]). **(d)** Temperature evolution of THz Hall conductivity at zero-field for *ab*-axis oriented Mn_3Ga sample.

tivity $\sigma_{xx}(\omega)$ are provided in figure S4 of the Supplementary Material [29].

Figure 4b shows the measured θ_f(1.5 THz) at discrete field values as the sample is magnetized through a field hysteresis of ±2.5 T at various temperatures. The *ab*-axis oriented Mn_3Ga film shows a significant θ_f at B=0 while it vanishes for the *c*-axis oriented Mn_3Ga film, consistent with the DC AHE observed in Fig.3a for these two crystal orientations. In the case of the *ab*-axis oriented Mn_3Ga film the measured $\theta_f(T)$ displays a non-monotonic behavior showing a maximum around 100 K. While this temperature evolution in *ab*-axis oriented sample qualitatively reflects a trend similar to DC AHE, DC and THz Hall components seem to peak at different points within the broad and slowly varying AHC signal with temperature. These observations from the Hall transport correlate well with the subtle features captured in the temperature evolution of magnetization in the same temperature range for the *ab*-axis sample. Further, we would like to point out that possible lattice distortions in this temperature range might induce a topological Hall component coming from spin canting in real space. The combined result of real and momentum space Hall components and their temperature evolution may result in a local maximum in the measured Hall signal in DC and THz probes.

Finally, to further confirm the correlation of DC and THz AHE, in Fig.4c we show the estimated magnitude of the THz AHC and its field evolution at 100 K. An entire hysteresis $\sigma_{xy}^{THz}(\omega = 0)$ with B is estimated by measuring $\theta_f(B)$, tracking the field-induced switching of AHE between ±4 T. Each data point in the $\sigma_{xy}^{THz}(\omega = 0)$ vs. B represents a linear extrapolation of $\sigma_{xy}(\omega)$ to its zero frequency value (see Figure S3, Supplementary Material [29]). As shown in Fig.4c and 4d, our result provides a qualitative agreement in the field and temperature evolution of AHC and a comparable magnitude[48] between DC and THz probes.

II.4. Magnetoresistance

An important aspect of the Weyl semimetals is their anisotropic magnetoresistance (MR). Particularly, the

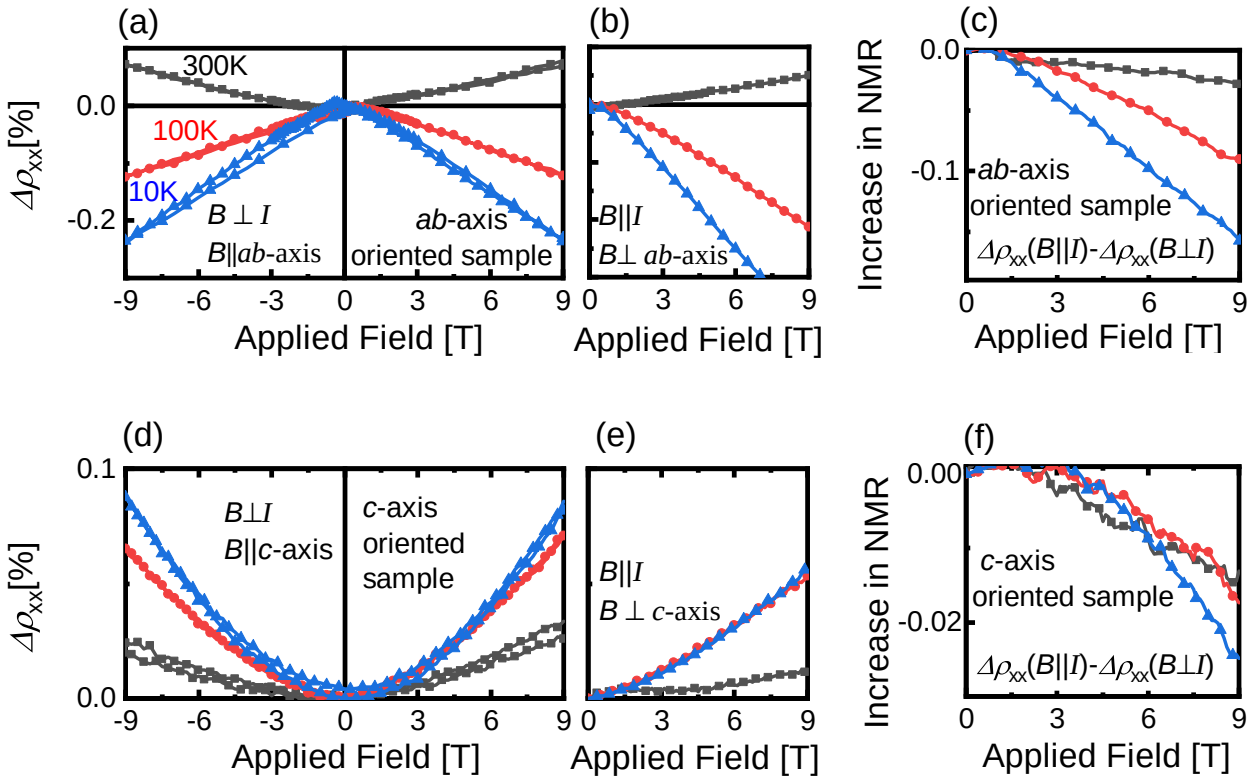

FIG. 5. **Magnetoresistance for *ab*-axis and *c*-axis oriented Mn_3Ga films. (a)-(b)** Magnetoresistance ($\Delta\rho_{xx} = [\rho_{xx}(B) - \rho_{xx}(B=0)]/100$) measured for *ab*-axis oriented Mn_3Ga film at various temperatures in B⊥I and B‖I configuration respectively. **(c)** Increase in negative magnetoresistance (NMR), the difference of the data shown in panels (a) and (b) estimated as $\Delta\rho_{xx}(B \parallel I) - \Delta\rho_{xx}(B \perp I)$ for *ab*-axis oriented Mn_3Ga film. **(d)-(e)** Magnetoresistance ($\Delta\rho_{xx}$) measured for *c*-axis oriented Mn_3Ga film at various temperatures in B⊥I and B‖I configuration respectively. **(f)** Increase in negative magnetoresistance, the difference of the data shown in panels (d) and (e), estimated as $\Delta\rho_{xx}(B \parallel I) - \Delta\rho_{xx}(B \perp I)$) for *c*-axis oriented Mn_3Ga film.

chiral anomaly is known to be a signature for the breakdown of the number conservation law of the left and right-handed Weyl fermions[13, 49]. This leads to the negative magnetoresistance (NMR) for B‖I configuration. In Figure 5 we show the MR measurements on the *ab*-axis (Figs.5a-5c) and *c*-axis (Figs.5d-5f) oriented Mn_3Ga films. Our films do not show a clear characteristic sign reversal of MR from positive to negative sign, with changing B⊥I to B‖I configuration. However, the quantitative evolution of MR with field suggests that there is a clear enhancement in NMR for B‖I case. This enhancement is quantified in Figs.5c and 5f as $\Delta\rho_{xx}(B \parallel I) - \Delta\rho_{xx}(B \perp I)$, which confirms the enhanced NMR for the entire temperature range. While our observation is suggestive of chiral anomaly, we point out that MR in these thin films may be sensitive to the band structure, field and temperature induced magnetic fluctuations, which are often present in the high field regime in these frustrated magnetic systems[49], leading to T-dependent spin scattering contributions. Such complex behavior of MR may mask the unambiguous identification of the chiral anomaly[1, 44].

Our results presented in Figs.5a-5b and 5d-5e reveal a distinct MR behaviour for *ab*-axis oriented sample compared and *c*-axis case. In the *ab*-axis sample the MR is dominated by field-linear term for both $B \parallel I$ and $B \perp I$ configurations, while in *c*-axis sample MR is dominated by the field-quadratic term. Further, this linear and quadratic field dependence of MR seems to evolve with temperature. It is suggested that a linear MR with field in these Mn_3X systems may be suggestive of type-2 Weyl fermions compared to field-linear dependence in type-1 Weyl fermions[49, 50]. Weyl fermions of type-2 are expected to emerge when there is a tilting of type-1 Weyl nodes, leading to distinct topological properties[51, 52]. Further, the effect of lattice strain along different crystal orientations may result in anisotropic modifications of bandstructure and hence transport signatures[52]. A detailed calculation of electronic band structure, a systematic investigation of lattice strain effects, and angular dependence of MR are essential for understanding the anisotropic MR behavior in these strained Mn_3Ga samples.

II.5. Exchange bias effect

The exchange bias (EB) effect is a result of magnetic coupling at the interface between a ferromagnetic (FM) and an antiferromagnet. A strong exchange coupling of

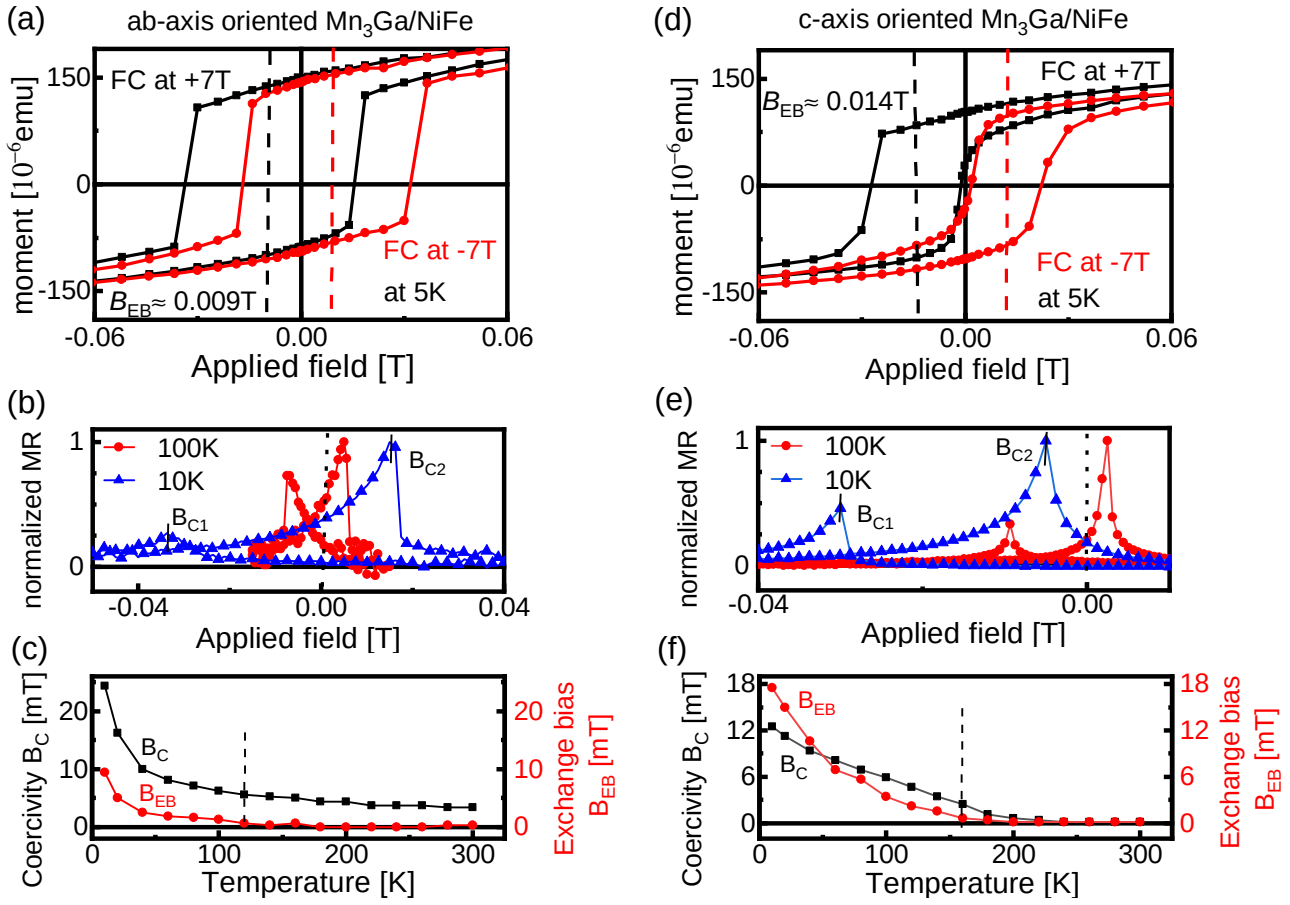

FIG. 6. **Exchange bias effect in Mn_3Ga(40 nm)/NiFe(10 nm) bilayers.(a)** Magnetization loop at 5 K for ±7 T cooling field conditions for *ab*-axis oriented Mn_3Ga(40 nm)/NiFe(10 nm) bilayer. **(b)** Normalized magnetoresistance (MR) measured for *ab*-axis oriented Mn_3Ga(40 nm)/NiFe(10 nm) bilayer at 100 K and 10 K. **(c)** Temperature evolution of exchange bias (B_{EB}) and coercivity (B_C) of the *ab*-axis oriented Mn_3Ga(40 nm)/NiFe(10 nm) bilayer estimated from MR measurements. **(d)** Magnetization loop at 5 K for ±7 T cooling field conditions for *c*-axis oriented Mn_3Ga(40 nm)/NiFe(10 nm) bilayer.**(e)** Normalized MR measured for *c*-axis oriented Mn_3Ga(40 nm)/NiFe(10 nm) bilayer at 100 K and 10 K. **(f)** Temperature evolution of B_{EB} and B_C of the *c*-axis oriented Mn_3Ga(40 nm)/NiFe(10 nm) bilayer estimated from MR measurements. Vertical dotted lines in panel (c) and (f) mark onset of exchange bias effect and the Blocking temperature.

the magnetic spins at the FM/AFM interface causes a delayed magnetization reversal of the FM layer, thereby shifting the FM hysteresis loop along the applied field axis. This interfacial effect is quantified by EB field (B_{EB}), a shift in M(B) loop along the applied field direction. Often an increase in coercivity (B_C) of the exchange-biased FM layer is also seen as a consequence of EB. However, B_C of an FM layer might be influenced by the microstructure of the layer itself, independent of the interface. Here a shift in M(B) loop quantified by B_{EB} provides a conclusive signature of the interfacial origin of EB. Further, the direction of the B_{EB} in the FM/AFM bilayer can be controlled by the direction of the applied cooling field, providing additional confirmation for the interfacial nature of the phenomenon.

Figures 6a and 6d show the magnetization with field (M(B)) for Mn_3Ga(40 nm)/NiFe(10 nm) bilayers at 5 K under different field-cooling (FC) protocols. A negative shift in the M(B) loop by 0.009 T and 0.014 T is witnessed under a positive cooling field with *ab*-axis and *c*-axis oriented Mn_3Ga, respectively. Upon reversing the cooling field from +7 T to ¬7 T, the shift in M(B) loop is shown to reverse its direction from the negative field axis to the positive.

To further probe the temperature evolution of B_C and B_{EB}, we measured the magnetoresistance of the Mn_3Ga/NiFe bilayers at various temperatures. Figures 6b and 6e show the normalized magnetoresistance data of NiFe(10 nm) at 10 K, 100 K interfaced with the *ab*-axis and *c*-axis oriented Mn_3Ga layers, respectively. Typical signatures for the EB effect are seen, namely, MR vs. B curves are shifted along the field axis, and the MR peak heights at B_{C1} and B_{C2} corresponding to the field sweeping down and sweeping up directions exhibit clear asymmetry[53–55]. One can estimate the layer B_C as the midpoint $|(B_{C2}+B_{C1})/2|$ of the descending and ascending branches, and a shift in the hysteresis loop, B_{EB} as $|(B_C - B_{C2}/2)|$.

In Figures 6c and 6f we track the evolution of the B_C and B_{EB} with varying temperatures between 10-300 K for both the *ab*-axis and *c*-axis oriented Mn_3Ga/NiFe bilayers. It is evident that NiFe interfaced with the *c*-axis oriented Mn_3Ga shows relatively a larger B_{EB} of 0.018 T at 10 K, which decreases slowly with temperature. On the other hand, with the *ab*-axis oriented Mn_3Ga film, the maximum B_{EB} of 0.01 T is observed at 10 K and rapidly decreases with increasing temperature. B_{EB} remains finite at least up to 160 K for the *c*-axis oriented Mn_3Ga while it vanishes beyond 100 K for the *ab*-axis oriented Mn_3Ga. Another noticeable observation is the enhancement of B_C for NiFe interfaced *ab*-axis oriented Mn_3Ga film compared to the *c*-axis case, which indicates the microstructural differences in NiFe layer, affected by the underlying layers. A larger magnitude of B_{EB} and its temperature extent for *c*-axis orientation compared to *ab*-axis case might indicate the distinct differences in magnetic coupling across Mn_3Ga/NiFe interface with varying crystal orientation of the AFM Mn_3Ga layer and the interfacial roughness. Notably, for NiFe grown *c*-axis oriented Mn_3Ga we expect the magnetization in NiFe to align parallel to the kagome spin structure formed in the underlying AFM. Such alignment of the easy axes of magnetization across the Mn_3Ga/NiFe interface may lead to a stronger magnetic coupling at the interface and hence a larger B_{EB}. For NiFe grown on *ab*-axis oriented Mn_3Ga film, we expect the easy axes of magnetization across the interface to be normal to each other leading to a decreased magnetic coupling and hence reduced B_{EB}. Our EB results confirm the interfacial magnetic interaction and the AFM nature of our Mn_3Ga films. Modeling these experimental observations through a detailed theoretical study may provide useful insights into the nature of magnetic domains, their stability, and the magnetic anisotropy in the 3 sub-lattice AFM Mn_3X systems.

III. CONCLUSIONS

In summary, we have developed high-quality epitaxial Mn_3Ga films by a sputtering method. Different crystal orientations of hexagonal Mn_3Ga films grown on suitable substrates and buffer layers are confirmed by detailed XRD and HRTEM investigations. The temperature-dependent large AHC in the *ab*-axis oriented AFM Mn_3Ga indicates its topological origin, and the enhanced negative MR for B‖I configuration points to a chiral anomaly, a signature of a Weyl semimetallic state. Field linear and quadratic dependence of MR, its anisotropy with crystal orientation, and effects of lattice strain need further theoretical and experimental insights. Large $T_N \approx 480$ K and the demonstration of EB effect further confirms the AFM nature of our films. Our observation of large optical AHE up to THz frequencies consistent with DC Hall transport highlights that our Mn_3Ga films are useful for developing future high-speed AFM spintronics.

IV. ACKNOWLEDGEMENT

The work at the Institute for Quantum Matter, an Energy Frontier Research Center was funded by DOE, Office of Science, Basic Energy Sciences under Award # DE-SC0019331. This work was partially supported by JST-Mirai Program (JPMJMI20A1), JST-CREST (JPMJCR18T3), and New Energy and Industrial Technology Development Organization (NEDO). The use of the facilities of the Materials Design and Characterization Laboratory at the Institute for Solid State Physics, The University of Tokyo, is gratefully acknowledged. This work was performed (in part) at the Materials Characterization and Processing Center in the Whiting School of Engineering at Johns Hopkins University.

[1] Armitage, N., Mele, E. & Vishwanath, A. Weyl and dirac semimetals in three-dimensional solids. *Reviews of Modern Physics* **90**, 015001 (2018).

[2] Baltz, V. *et al.* Antiferromagnetic spintronics. *Reviews of Modern Physics* **90**, 015005 (2018).

[3] Nakatsuji, S. & Arita, R. Topological magnets: Functions based on Berry phase and multipoles. *Annual Review of Condensed Matter Physics* **13**, 119–142 (2022).

[4] Šmejkal, L., MacDonald, A. H., Sinova, J., Nakatsuji, S. & Jungwirth, T. Anomalous hall antiferromagnets. *Nature Reviews Materials* **7**, 482–496 (2022).

[5] Nakatsuji, S., Kiyohara, N. & Higo, T. Large anomalous hall effect in a non-collinear antiferromagnet at room temperature. *Nature* **527**, 212–215 (2015).

[6] Matsuda, T. *et al.* Room-temperature terahertz anomalous hall effect in weyl antiferromagnet mn3sn thin films. *Nature communications* **11**, 1–8 (2020).

[7] Kimata, M. *et al.* Magnetic and magnetic inverse spin hall effects in a non-collinear antiferromagnet. *Nature* **565**, 627–630 (2019).

[8] Ikhlas, M. *et al.* Large anomalous nernst effect at room temperature in a chiral antiferromagnet. *Nature Physics* **13**, 1085–1090 (2017).

[9] Mizuguchi, M. & Nakatsuji, S. Energy-harvesting materials based on the anomalous nernst effect. *Science and technology of advanced materials* **20**, 262–275 (2019).

[10] Higo, T. *et al.* Large magneto-optical kerr effect and imaging of magnetic octupole domains in an antiferromagnetic metal. *Nature photonics* **12**, 73–78 (2018).

[11] Wu, M. *et al.* Magneto-optical Kerr effect in a noncollinear antiferromagnet Mn_3Ge. *Appl. Phys. Lett.* **116** (2020).

[12] Zhao, H. *et al.* Large ultrafast-modulated voigt effect in noncollinear antiferromagnet mn3sn. *Nature communications* **12**, 1–8 (2021).

[13] Chen, T. *et al.* Anomalous transport due to weyl fermions in the chiral antiferromagnets mn3x, x= sn, ge. *Nature communications* **12**, 1–14 (2021).

[14] Higo, T. & Nakatsuji, S. Thin film properties of the non-collinear Weyl antiferromagnet Mn_3Sn. *J. Magn. Magn. Mater.* **564**, 170176 (2022).

[15] Zhang, Y. *et al.* Strong anisotropic anomalous hall effect and spin hall effect in the chiral antiferromagnetic compounds mn 3 x (x= ge, sn, ga, ir, rh, and pt). *Physical Review B* **95**, 075128 (2017).

[16] Tomiyoshi, S., Abe, S., Yamaguchi, Y., Yamauchi, H. & Yamamoto, H. Triangular spin structure and weak ferromagnetism of mn3sn at low temperature. *Journal of Magnetism and Magnetic Materials* **54-57**, 1001–1002 (1986). URL `https://www.sciencedirect.com/science/article/pii/0304885386903537`.

[17] Chen, Y. *et al.* Antichiral spin order, its soft modes, and their hybridization with phonons in the topological semimetal mn_3Ge. *Phys. Rev. B* **102**, 054403 (2020). URL `https://link.aps.org/doi/10.1103/PhysRevB.102.054403`.

[18] Takeuchi, Y. *et al.* Chiral-spin rotation of non-collinear antiferromagnet by spin–orbit torque. *Nature Materials* **20**, 1364–1370 (2021).

[19] Higo, T. *et al.* Perpendicular full switching of chiral antiferromagnetic order by current. *Nature* **607**, 474–479 (2022).

[20] Hong, D. *et al.* Large anomalous nernst and inverse spin-hall effects in epitaxial thin films of kagome semimetal mn 3 ge. *Physical Review Materials* **4**, 094201 (2020).

[21] Tsai, H. *et al.* Electrical manipulation of a topological antiferromagnetic state. *Nature* **580**, 608–613 (2020).

[22] Xie, H. *et al.* Magnetization switching in polycrystalline mn3sn thin film induced by self-generated spin-polarized current. *Nature Communications* **13**, 1–10 (2022).

[23] Chen, X. *et al.* Octupole-driven magnetoresistance in an antiferromagnetic tunnel junction. *Nature* **613**, 490–495 (2023).

[24] Matsuda, T. *et al.* Ultrafast dynamics of intrinsic anomalous hall effect in the topological antiferromagnet mn 3 sn. *Physical review letters* **130**, 126302 (2023).

[25] Jeon, K.-R. *et al.* Long-range supercurrents through a chiral non-collinear antiferromagnet in lateral josephson junctions. *Nature materials* **20**, 1358–1363 (2021).

[26] Liu, Z. *et al.* Transition from anomalous hall effect to topological hall effect in hexagonal non-collinear magnet mn3ga. *Scientific Reports* **7**, 1–7 (2017).

[27] Hu, F. *et al.* Tunable magnetic and transport properties of mn3ga thin films on ta/ru seed layer. *Journal of Applied Physics* **123**, 103902 (2018).

[28] Cheng, B. *et al.* Terahertz conductivity of the magnetic weyl semimetal mn3sn films. *Applied Physics Letters* **115**, 012405 (2019).

[29] See supplementary material for the experimental methods related to thin film growth, structural characterization of the thin films using x-ray diffraction, high-resolution transmission electron microscopy, magnetic characterization using magnetic property measurement system, magnetotransport characterization using physical property measurement system, optical characterization using tera-hertz optical and faraday effects, additional data on rocking curve measurements, temperature-dependent dc transport, frequency-dependent faraday effect and thz optical conductivity are provided, supplementary material also contains ref. [19, 28, 34] .

[30] Boeije, M., van Eijck, L., van Dijk, N. & Brück, E. Structural and magnetic properties of hexagonal (mn, fe) 3-δga. *Journal of Magnetism and Magnetic Materials* **433**, 297–302 (2017).

[31] You, Y. *et al.* Room temperature anomalous hall effect in antiferromagnetic mn3snn films. *Applied Physics Letters* **117**, 222404 (2020).

[32] Boldrin, D. *et al.* Giant piezomagnetism in mn3nin. *ACS applied materials & interfaces* **10**, 18863–18868 (2018).

[33] Yoon, J. *et al.* Crystal orientation and anomalous hall effect of sputter-deposited non-collinear antiferromagnetic mn3sn thin films. *Applied Physics Express* **13**, 013001 (2019).

[34] Seto, Y. & Ohtsuka, M. ReciPro: free and open-source multipurpose crystallographic software integrating a crystal model database and viewer, diffraction and microscopy simulators, and diffraction data analysis tools. *J. Appl. Cryst.* **55**, 397–410 (2022).

[35] Markou, A. *et al.* Noncollinear antiferromagnetic mn 3 sn films. *Physical Review Materials* **2**, 051001 (2018).

[36] Ikhlas, M. *et al.* Piezomagnetic switching of the anomalous hall effect in an antiferromagnet at room temperature. *Nature Physics* **18**, 1086–1093 (2022).

[37] Niida, H., Hori, T. & Nakagawa, Y. Magnetic properties and crystal distortion of hexagonal mn3 ga. *Journal of the Physical Society of Japan* **52**, 1512–1514 (1983).

[38] Song, L. *et al.* Observation of structural distortion and topological hall effect in noncollinear antiferromagnetic hexagonal mn3ga magnets. *Applied Physics Letters* **119**, 152405 (2021).

[39] Kan, D. & Shimakawa, Y. Strain effect on structural transition in srruo3 epitaxial thin films. *Crystal growth & design* **11**, 5483–5487 (2011).

[40] Nayak, A. K. *et al.* Large anomalous hall effect driven by a nonvanishing berry curvature in the noncolinear antiferromagnet mn3ge. *Science advances* **2**, e1501870 (2016).

[41] Meng, Q. *et al.* Magnetostriction, piezomagnetism and domain nucleation in mn ̲3 sn. *arXiv preprint arXiv:2301.06401* (2023).

[42] Zelenskiy, A., Monchesky, T., Plumer, M. & Southern, B. Anisotropic magnetic interactions in hexagonal a b-stacked kagome lattice structures: Application to mn 3 x (x= ge, sn, ga) compounds. *Physical Review B* **103**, 144401 (2021).

[43] Kiyohara, N., Tomita, T. & Nakatsuji, S. Giant anomalous hall effect in the chiral antiferromagnet mn 3 ge. *Physical Review Applied* **5**, 064009 (2016).

[44] Khadka, D. *et al.* Kondo physics in antiferromagnetic weyl semimetal mn3+ x sn1- x films. *Science advances* **6**, eabc1977 (2020).

[45] Higo, T. *et al.* Omnidirectional control of large electrical output in a topological antiferromagnet. *Adv. Funct. Mater.* **31**, 2008971 (2021).

[46] Krén, E. & Kádár, G. Neutron diffraction study of mn3ga. *Solid State Communications* **8**, 1653–1655 (1970).

[47] Li, X., Koo, J., Zhu, Z., Behnia, K. & Yan, B. Field-linear anomalous hall effect and berry curvature induced by spin chirality in the kagome antiferromagnet mn3sn. *Nature Communications* **14**, 1642 (2023).

[48] Bhandia, R. *et al.* Thz-range faraday rotation in the weyl semimetal candidate co2tige. *Journal of Applied Physics* **128**, 244303 (2020).

[49] Kuroda, K. *et al.* Evidence for magnetic weyl fermions in a correlated metal. *Nature materials* **16**, 1090–1095 (2017).

[50] Zyuzin, V. A. Magnetotransport of weyl semimetals due to the chiral anomaly. *Physical Review B* **95**, 245128

(2017).

[51] Udagawa, M. & Bergholtz, E. J. Field-selective anomaly and chiral mode reversal in type-ii weyl materials. *Physical review letters* **117**, 086401 (2016).

[52] Soluyanov, A. A. *et al.* Type-ii weyl semimetals. *Nature* **527**, 495–498 (2015).

[53] Hoffmann, A. Symmetry driven irreversibilities at ferromagnetic-antiferromagnetic interfaces. *Physical review letters* **93**, 097203 (2004).

[54] Brems, S., Temst, K. & Van Haesendonck, C. Origin of the training effect and asymmetry of the magnetization in polycrystalline exchange bias systems. *Physical review letters* **99**, 067201 (2007).

[55] Radu, F. *et al.* Interfacial domain formation during magnetization reversal in exchange-biased coo/co bilayers. *Physical Review B* **67**, 134409 (2003).